When Quantum Fluctuations Meet Structural Instability: The Isotope- and Pressure-Induced Phase Transition in the Quantum Paraelectric NaOH

SUPPLEMENTAL MATERIAL

Sofiane Schaack,[1] Etienne Mangaud,[1,2] Erika Fallacara,[1] Simon Huppert,[1] Philippe Depondt,[1] and Fabio Finocchi[1]

[1] *Sorbonne Université, CNRS UMR 7588, Institut des NanoSciences de Paris, INSP, 75005 Paris, France*
[2] *Univ Gustave Eiffel, Univ Paris Est Créteil, CNRS, UMR 8208, MSME, F-77454 Marne-la-Vallée, France*

A. Computational Details: Electronic Structure

In the DFT calculations, we mainly employ the PBE approximation to the exchange-correlation energy. Among other GGA approximations, the PBE is known to describe hydrogen bonds quite well, with a slight tendency to overestimate their strength in several molecules and solids [1, 2]. Within the PBE approximation, the iono-covalent OH bond in the isolated water molecule is longer than the experimental value. The latter drawback is fairly eliminated when using a hybrid correction, that is, the PBE0 approximation [3]. In order to assess the impact of the chosen exchange-correlations approximations on the energetics of sodium hydroxide, we report in section C an extensive comparison of selected configurations that are computed either at the PBE or the PBE0 levels. We anticipate that the energy differences of the relevant configurations does not vary significantly (see section C). For computational reasons, we employed the PBE in all the dynamical calculations, as the use of PBE0 can slow down the computational time needed for the convergence of the Kohn-Sham equations roughly by an order of magnitude.

In the electronic structure calculations adopting the PBE functional, we employ ultra-soft (US) pseudopotentials for O and H and include the semi-core $2s$ and $2p$ Na electrons in the self-consistent charge density, using a plane-wave expansion cutoff of 60 Ry for the Kohn-Sham states and 8 times as large for the charge and the potential. In order to check the influence of the pseudopotentials, we optimized several distinct configurations (AFE, FE, PE as described in section B) by using optimized norm-conserving pseudopotentials (ONC) [4] with a 90 Ry cutoff for the Kohn-Sham states and 360 Ry for the charge and the potential, either in the PBE or in the hybrid PBE0 approximations. The optimized structures are very similar as far as the equilibrium lattice parameters, bond lengths and OH slanted angle θ are concerned. The total energy behaves quantitatively the same as a function of the c lattice parameter.

In order to represent both antiferro-electric (AFE) and ferro-electric (FE) configurations in a single computational setup, we considered a cell with doubled lattice parameter $2a$. We use orthorhombic cells containing 8 NaOH (NaOD) units ($2a \simeq 6.9$ Å, $b \simeq 3.4$ Å, 9.6 Å $\leq c \leq$ 13.7 Å), with $\mathbf{a} \parallel \hat{x}$, $\mathbf{b} \parallel \hat{y}$, and $\mathbf{c} \parallel \hat{z}$. We adopt a $(2, 3, 1)$ k-point sampling centred at Γ. A finer k-point sampling does not influence significantly the energy differences between the NaOH structures that are sketched in Fig. B and we considered as benchmarks.

B. OH ordering.

From structural optimization at $T = 0$ K, we can distinguish several local minima, differing by the alignment of the hydroxyl groups. The main ones are drawn in Fig.1. Top left, the most stable antiferro-electric (AFE) structure: the OH groups lie in the (**bc**) plane and form hydrogen bonds between successive NaOH stacks along **c**; the OH groups are antiparallel when considering neighboring chains along the **a** axis. In the ferro-electric (FE) configuration (bottom, left), the OH groups are all parallel to each other. By doubling the dimension of the unit cell along (**c**), we also considered an intermediate structure between the AFE and FE, the in-plane FE/out-of-plane AFE (top, right), in which the hydroxyl groups are all parallel within the (**bc**) plane, while they are antiparallel when moving along **c**. This structure is almost degenerate with the FE one, which shows that the ordering of the HBs on different stacks is secondary with respect to the ordering of HBs in antiparallel chains when moving along (**a**).

In all of the three AFE, FE and the in-plane FE/out-of-plane AFE configurations, hydrogen bonds are formed between two successive NaOH bilayers; the OH groups form an angle $\pm\theta$ with the **c** axis. In the para-electric (PE) structure (bottom, right), the OH are all parallel to the **c** axis ($\theta = 0$) and do not form hydrogen bonds between the NaOH bilayers. Along the dynamics and depending on the temperature, the orientation of the OH groups can be considered as a statistical mix of the four configurations here depicted (see, e.g. Fig.5 in the main text).

C. Potential Energy Surfaces

The potential energy surface $E(\theta, c)$ that is shown in Fig.1 (b) in the main text was computed by constrained structural optimizations at fixed hydroxyl angle θ and

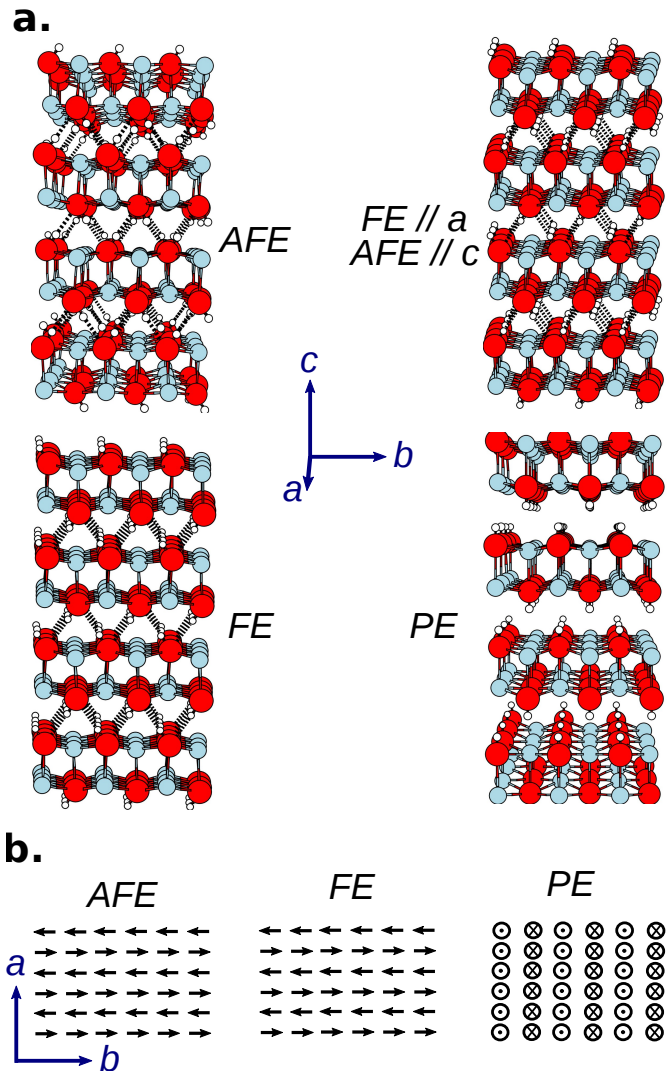

FIG. 1. OH ordering in four different structures: antiferro-electric (AFE), mixed antiferro-ferro-electric (FE parallel to the **a.** axis, AFE parallel along the **c** axis, ferro-electric (FE), and para-electric (PE). Panel **a**: atomic structures, Na are in light blue, O in red and H in white. Hydrogen bonds are drawn as dashed lines. The directions of the **a, b, c** vectors are indicated as blue arrows. Panel **b.** schematic representation of the OH-dipole orientation projected in the **ab**-plane for the three relevant in-plane ferro-electric order configurations.

lattice parameters for the AFE configuration, by varying θ in the $(-50°, 50°)$ range and $c \in (9.8, 12.6)$ Å.

By relaxing the constraint on the θ angle, the potential energy surface becomes a function of the lattice parameter c. Depending on the initial choice of the OH orientations, we obtained distinct curves for the AFE, FE and PE configurations, which correspond to distinct space groups. Moreover, we conducted a detailed comparison between the PBE generalized gradient and PBE0 hybrid approximations to the exchange and correlation energy (Fig. 2).

In the PBE calculations, the lattice parameters a and b, as well as the atomic positions, are fully optimized in each configuration and for each c value. At the PBE0 level, the a and b lattice parameters are fixed at their PBE values [5], while the atomic positions are fully relaxed. The resulting PBE and PBE0 curves are very similar: the AFE configuration is slightly more stable than the FE one, for all c values. Their minima are at $c_0 \simeq 10.37$ Å; $E_{\rm FE}(c_0) - E_{\rm AFE}(c_0) = 3.5$ meV/unit within the PBE and 2.5 meV/unit at the PBE0 level. For this value of the c lattice parameter, the para-electric configuration is higher in energy by about 40-50 meV/unit, that is, roughly twice the thermal energy at room temperature.

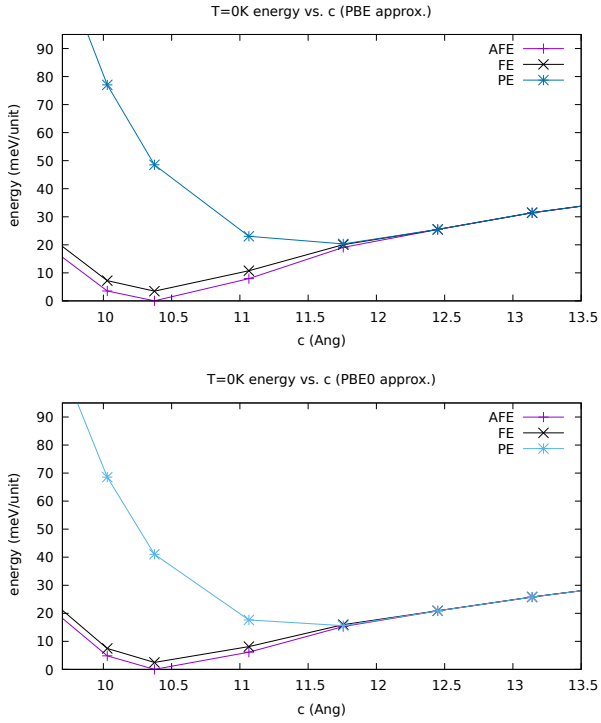

FIG. 2. $T = 0$ K energy versus lattice parameter c in the PBE (upper frame) and PBE0 approximations (lower frame). The energy is plotted separately for the antiferro-electric (AFE), ferro-electric (FE), and para-electric (PE) configurations.

Both AFE and FE curves merge into the PE one around $c \simeq 12$ Å, very close to the minimum of the PE energy curve, in both PBE and PBE0 approximations. We can conclude that the potential energy surfaces that are relevant for the dynamics are very close at PBE and PBE0 theory levels.

We then focus on the lowest-energy curve $E_0(c)$, that corresponds to the AFE configuration for $c \leq 12$ Å and PE configuration for for $c > 12$ Å, both in PBE and PBE0 . $E_0(c)$ can be fitted via a Morse potential $V_0(c) = D_0(1 - {\rm e}^{-(c-c_0)/\lambda})^2$, with $D_0 = 0.30$ eV, $c_0 = 10.37$ Å and $\lambda = 1.15$ Å. Hence, $E_0(c)$ adheres to a universal binding curve that has been originally proposed for metallic binding [6] and then extended to carbon-based systems with strong covalent bonds [7, 8]. In all

these cases, the binding energy is given as a function of an inter-atomic distance or, when possible, a lattice parameter. The bond rupture occurs at the inflexion point of the energy versus distance curve; in the case of sodium hydroxide, the critical lattice parameter is $c_{cr} = c_0 + \lambda \ln 2 \simeq 11.2$Å, which corresponds to a maximum for the inter-layer attractive force that occurs at a given threshold value $(\text{O..H})_{cr}$ of the Hydrogen bond length. For further expansion beyond c_{cr}, the inter-layer attractive force weakens, which causes rupture.

In order to validate such a picture, we compute the static elastic constants in the PBE approximation at varying c lattice parameter: first, the structure is fully optimized at constrained c in the lowest-energy PES; then, for each c, we vary the lattice parameters (the typical deformations are 0.5%) and, by interpolation of the stress-strain relation, we compute the static $C_{ij}^{(0)}$ elastic constants that are shown in Fig. 3. For $c > c_{cr}$, $C_{33}^{(0)}$ becomes negative (see Fig.3), which is a fingerprint of the mechanical instability of the AFE and FE PES [9].

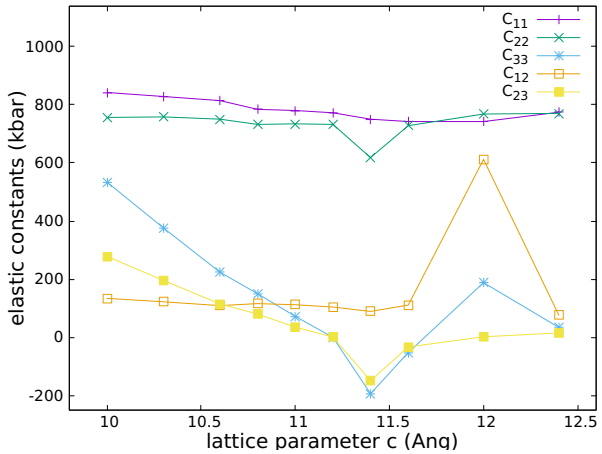

FIG. 3. Static $C_{ij}^{(0)}$ elastic constant as computed from fully relaxed PBE calculations at fixed lattice parameter c (see text for computational details).

Notably, $E_0(c_{cr})$ lies about 12 meV below the corresponding energy for the para-electric configuration $E_{\text{PE}}(c_{cr})$. Such a difference corresponds to about 150 K, and temperature fluctuations can easily drive the AFE configuration towards higher lattice parameters than c_{cr} and eventually to PE-like configurations. The static elastic constant softening and the concomitant proximity of the para-electric potential energy surface are at the root of the mechanical instability of the AFE configuration.

As the hydrogen bond length (O..H) is directly correlated to the c lattice parameter (see section D), the potential $V_0(c)$ provides a criterion to pinpoint hydrogen bond breaking in NaOH at its inflexion point.

D. O-H bond lengths and O-O distances

The minimum of $E_0(c)$ occurs at $c_0 = 10.375$ Å. For this value, the short (iono-covalent) OH bond length is 0.984 Å and the hydrogen bond length (O..H)=2.05 Å, at the PBE level. Upon increasing lattice parameter c, the hydrogen bond weakens considerably (see Fig. 4, lower panel). Concomitantly, the iono-covalent OH bond shortens and reaches a plateau at 0.975 Å at $c \geq 12$ Å in the para-electric configuration, where hydrogen bonds are fully broken. Within the hybrid PBE0 approximation, the iono-covalent OH bond is shortened by $\simeq 1\%$ and the hydrogen bond is very slightly expanded with respect to the PBE. Thus, the inclusion of a fraction of exact exchange corrects the typical PBE drawback, providing shorter OH bond lengths, that are likely closer to the (unknown) experimental values in NaOH and NaOD. The trend for the hydrogen bond length is very similar in the two approximations, especially above the critical value $c_{cr} = 11.2$ Å; as a consequence, the weakening and the rupture of the hydrogen bonds, at least at the static level, is expected to be described in the same way in both PBE and PBE0 approximations.

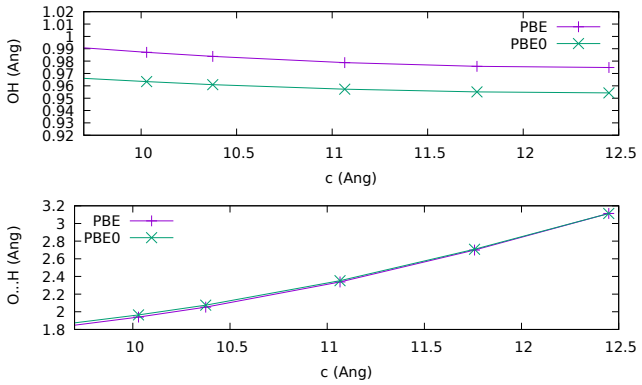

FIG. 4. O-H bond lengths versus the lattice parameter c, in the PBE and PBE0 approximations. Top panel: the (short) ionio-covalent OH bond length. Bottom panel: the hydrogen bond length (O..H). Both graphs refer to the most stable configuration at the lattice parameter c.

When the crystal is elongated along the c axis, one expects that the inter-layer O-O distance stretches, as do hydrogen bonds. Using full lattice relaxation at constrained lattice parameters in DFT optimization runs at $T = 0$ K, we confirm that there is a monotonic relation between the lattice parameter c and the inter-layer O-O distance d_{OO} (Fig. 5).

At the critical value c_{cr} corresponding to the inflection point of the Morse curve $V_0(c)$ (see section B), the inter-layer O-O distance is $d_{\text{OO}\ (cr)}$ =3.41 Å and the corresponding hydrogen bond length is $(\text{O..H})_{(cr)} = 2.42$ Å with 168.7° OHO angle.

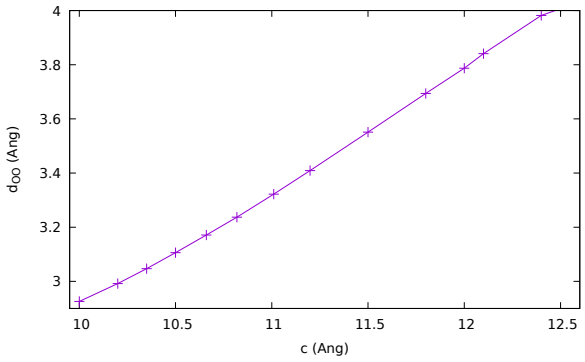

FIG. 5. Inter-layer O-O distance in classical NaOH at $T = 0$ K versus the lattice parameter c. Results are obtained via PBE optimization runs at constrained lattice parameter c.

E. Dynamical Runs

The path-integral simulations were carried out using the PIGLET thermostat from the i-PI package[10], with a timestep of 0.48fs and 24 beads; we carefully checked convergence of the kinetic and potential energies at 77K.

We first performed series of (NVT) trajectories (either 15 ps with a classical Langevin thermostat or 5 ps with the PIGLET method to account for quantum effects) by varying the a, b, c lattice parameters independently in order to estimate the elastic constants C_{ij} from the stress-strain relation. We varied a and b by $\simeq 0.5\%$ and c up to 4%, as the C_{33} and C_{23} elastic constants are significantly lower (by an order of magnitude) than C_{11} and C_{22}. Once the elastic constant matrix has been determined, we estimated its inverse (the elastic compliance matrix) and the equilibrium lattice parameters $a_0(T)$, $b_0(T)$, $c_0(T)$. They are reported in Tab.I as a function of T in both NaOH and NaOD. Through a final run at $a_0(T)$, $b_0(T)$, $c_0(T)$, we checked that the absolute diagonal stress components $|\sigma_{ii}| < 1$ kbar.

TABLE I. Optimized NaOD lattice parameters a_0, b_0, c_0, in Å and diagonal components σ_{ii} of the residual stress in kbar as obtained from PIGLET runs at varying temperature. All results refer to the orthorhombic cell.

T (K)	a_0	b_0	c_0	σ_{11}	σ_{22}	σ_{33}
77	3.463	3.398	10.60	0.1	-0.8	-0.2
150	3.458	3.401	10.76	0.3	0.0	-0.5
200	3.460	3.405	10.85	-0.2	-0.2	-0.0
250	3.459	3.410	10.96	-0.2	0.1	0.3
300	3.435	3.415	11.65	0.2	0.2	0.7
350	3.435	3.414	11.60	-0.7	-0.4	-0.0

The statistical uncertainty on the stress tensor over such short trajectories is indeed of the order of ± 0.5 kbar. This implies error bars of the order of few tens of kbar on the numerical estimates of the elastic constants. By error propagation, we estimated the error bars on the equilibrium lattice parameters $a_0(T)$, $b_0(T)$, $c_0(T)$ that

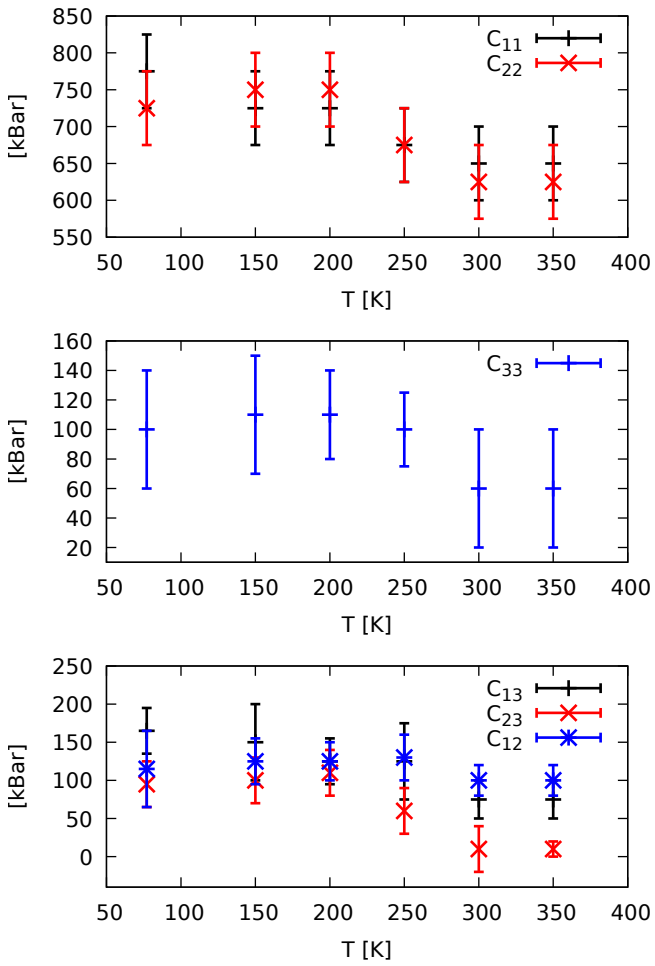

FIG. 6. Elastic constants C_{ij} in kbar for NaOD, versus temperature, as obtained from PIGLET runs as explained in the text.

TABLE II. Optimized NaOH lattice parameters a_0, b_0, c_0, in Å and diagonal components σ_{ii} of the residual stress in kbar as obtained from PIGLET runs at varying temperature. All results refer to the orthorhombic cell.

T (K)	a_0	b_0	c_0	σ_{11}	σ_{22}	σ_{33}
100	3.415	3.393	11.35	-0.1	0.2	0.3
200	3.427	3.404	11.45	-0.6	-0.2	-0.0
300	3.434	3.415	11.60	-0.3	0.0	0.4

are reported in Fig.2 of the main text. As C_{33} is much smaller than both C_{11} and C_{22}, (see Fig.6) the error bar on $c_0(T)$ is noticeably larger than that on the other lattice parameters.

In order to determine how lattice parameters vary with the temperature in the classical framework, we run classical Langevin simulations (with a friction coefficient of 12ps^{-1} and a time step of 0.5 fs) in the range 77 K $\leq T \leq$ 400 K. The evolution of the lattice parameters is smooth up to 350 K. Between 350 and 400 K, a contracts by

TABLE III. Optimized NaOH/NaOD lattice parameters a_0, b_0, c_0, in Å and diagonal components σ_{ii} of the residual stress in kbar as obtained from **classical** Langevin runs at varying temperature. All results refer to the orthorhombic cell.

T (K)	a_0	b_0	c_0	σ_{11}	σ_{22}	σ_{33}
77	3.466	3.390	10.36	0.1	0.2	0.0
150	3.467	3.398	10.52	0.4	-0.2	0.0
200	3.469	3.406	10.66	0.2	-0.3	-0.4
250	3.469	3.413	10.86	-0.7	-0.4	-0.1
300	3.470	3.422	11.00	-0.7	-0.3	0.2
350	3.469	3.429	11.22	-0.6	0.3	-0.2
400	3.456	3.437	11.65	-0.2	0.5	-0.2

0.01 Å and the coefficient of thermal expansion along c clearly increases, although in the classical frame we did not detect such a sudden jump as for NaOD within the path-integral-based simulations. Interestingly, at 400 K, the values of c as obtained by PIMD for NaOH, NaOD and classical Langevin simulations coincide within the error bar, showing that at this temperature the quantum and classical descriptions converge.

F. Angular distributions and free energy

The angular distributions $p(\theta;T)$ that we obtained from the classical Langevin simulations at the equilibrium lattice parameters for each temperature (listed in Tab.III) are shown in Fig.7. They switch from a distribution with two well split maxima at 77 K to a unimodal distribution at 400 K.

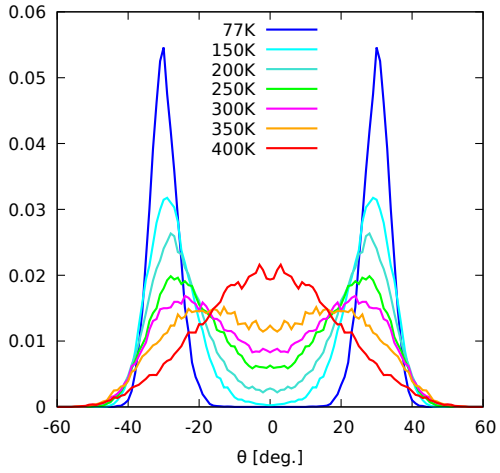

FIG. 7. Distributions of the polar angle θ as extracted from classical Langevin MD simulations at various temperatures.

From the (θ_1, θ_2) joint distributions (Fig.8), the classical system can be characterized as a perfect AFE at 77 K. Upon increasing temperature, the FE configuration $(\theta_1 \simeq \theta_2 \simeq 30°)$ progressively appears beside the AFE one, until at 300 K both AFE and FE ordering coexist with similar probabilities. The minimum that is still visible at 350K around the PE configuration $(\theta_1 \simeq \theta_2 \simeq 0°)$ becomes a maximum for $T = 400$ K, where the classical system reaches a dynamical para-electric state. The AFE/PE transition is rather progressive in the classical framework as compared to the quantum results for NaOD presented in the main text.

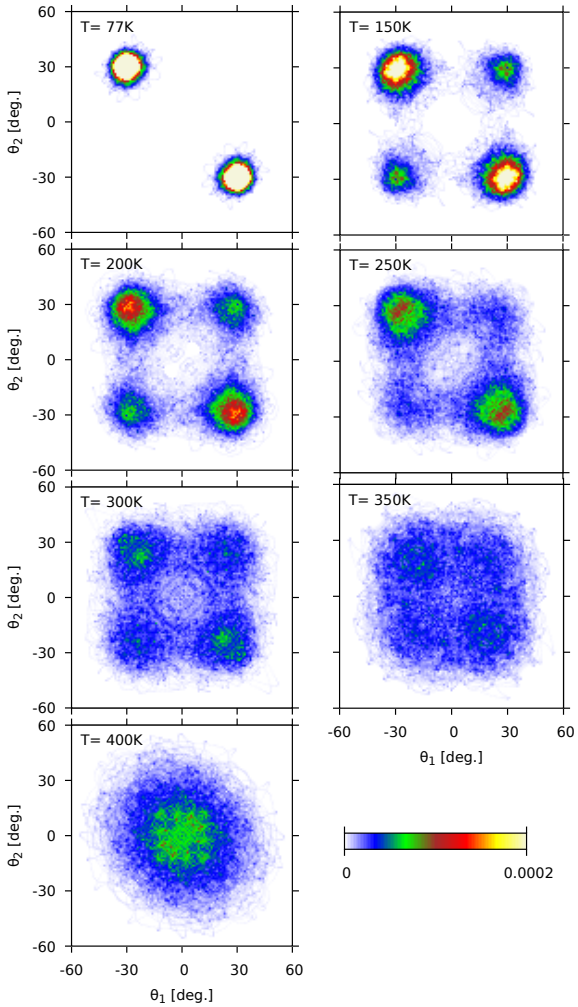

FIG. 8. Joint probability distribution of the polar angles of hydroxyl groups at $x=0$ (θ_1) and $x=1/2$ (θ_2) in sodium hydroxide as extracted from classical Langevin MD simulations at various temperatures.

We show in figure 9 the free energy profile $F(\theta, T) = -RT \log p(\theta;T)$ as extracted from the marginal probability distributions as functions of the order parameter θ in the PIMD simulations (Fig. 3 of the main text), for NaOH and NaOD.

At low temperatures, the NaOD free energy displays two minima: at $T = 77$ K they are well split by a significant energy barrier $\simeq 275$ K, which reduces down to 160 K at $T = 250$ K. The curves at 300 and 350 K show a single minimum, which is consistent with the transition to a thermally activated paraelectric between 250 and 300 K, within our approximations.

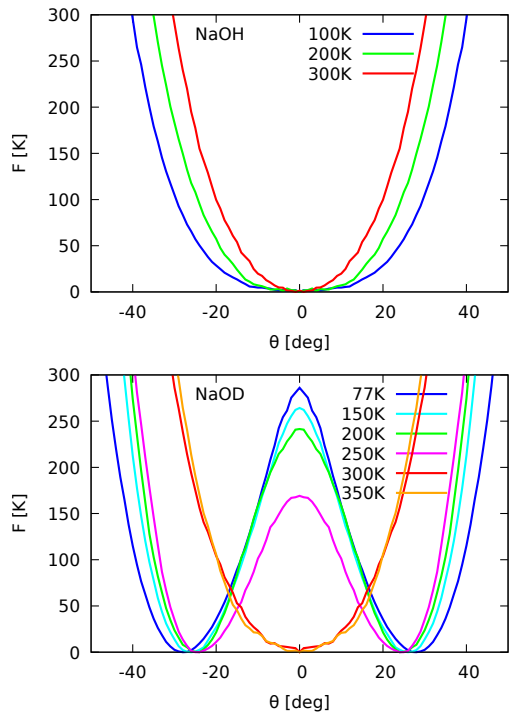

FIG. 9. Free energy expressed in K as a function of angle θ and temperature for NaOH and NaOD (PIMD simulations). The energy origins are arbitrary.

In contrast, NaOH shows a single minimum at $\theta = 0$ in all the explored T range up to 300K. Interestingly, the width of the NaOH free-energy profile is almost independent of temperature, which is characteristic of a quantum paraelectric [11].

At high temperatures the $F(\theta, T)$ curves are very similar for NaOH and NaOD, which shows that isotope effects vanish at room temperature. Within the PBE approximation, at $T \geq 300$ K the sodium hydroxide crystal becomes a paraelectric where faint hydrogen bonds are no more stable and fully overwhelmed by thermal fluctuations. The classical distributions around 400 K converge to their room-T PIMD counterparts.

G. Dielectric matrix and effective charges

We computed, from the Density Functional Perturbation Theory in the harmonic approximation [12], the dielectric and the atomic effective charge tensors, in both AFE and PE configurations (see Tab.IV). Each configuration is in its fully relaxed state at $T = 0$ K, with the optimized lattice parameters as listed in Tab.1 of the main text.

We note that the zz component of the H effective charge (along the c axis) is almost null in the paraelectric phase, whereas it amounts to $\simeq 0.43$ in the AFE phase. Accordingly, the zz component of the O effective charge passes from -1.087 (PE) to -1.473 (AFE). Therefore, the existence of hydrogen bonds in the AFE configuration implies a significant variation of the dipole moment normal to the NaOH stacks when the proton moves along z. This is not the case for the PE configuration. Smaller variations between the AFE and PE configurations are also visible on the xx and yy components of the effective charge tensors.

TABLE IV. Diagonal components of the dielectric tensor ϵ_∞ and the effective charge tensors $Z^*_{\rm Na}$, $Z^*_{\rm O}$ and $Z^*_{\rm H}$ for antiferroelectric (AFE) and para-electric (PE) configurations.

	xx	yy	zz
ϵ_∞ (AFE)	2.28	2.38	2.35
ϵ_∞ (PE)	2.25	2.37	2.22
$Z^*_{\rm Na}$ (AFE)	1.015	0.974	1.050
$Z^*_{\rm Na}$ (PE)	0.981	0.962	1.049
$Z^*_{\rm O}$ (AFE)	-1.243	-1.435	-1.473
$Z^*_{\rm O}$ (PE)	-1.260	-1.379	-1.087
$Z^*_{\rm H}$ (AFE)	0.218	0.451	0.428
$Z^*_{\rm H}$ (PE)	0.273	0.407	0.043

The total static dielectric constant ϵ_0 is the sum of the purely electronic contribution ϵ_∞ and a contribution of the ionic response to a static electric field [13]:

$$\epsilon_{0,\alpha\beta} = \epsilon_{\infty,\alpha\beta} + \frac{4\pi}{\Omega} \sum_{l,\kappa,\gamma} Z^*_{\kappa,\gamma\alpha} \frac{\partial \tau_{l,\kappa,\gamma}}{\partial \mathcal{E}_\beta} \qquad (1)$$

where $\alpha, \beta, \gamma = x, y, z$, $\tau_{l,\kappa}$ is the position of the ion κ within the $l^{\rm th}$ cell, Ω the unit cell volume and $\mathcal{E}$ the electric field. A significant contribution to the variation of the static dielectric constant is therefore due to the decrease of the O and H zz components of the effective charge tensor, which affects the ionic part. As far as the electronic contribution ϵ_∞ to the dielectric tensor is concerned, there is a $\simeq 5\%$ reduction of the zz component in the PE with respect to the AFE configuration, which can be related to the lack of hydrogen bonds.

[1] L. Rao, H. Ke, G. Fu, X. Xu, and Y. Yan, J. Chem. Th. Comp. **5**, 86 (2009).

[2] L. Gasparic, P. M., and A. Kokalj, Chem. Phys. **559**, 111539 (2022).

[3] M. Gillan, D. Alfè, and A. Michaelides, Perspective: How good is dft for water?, J. Chem. Phys. **144**, 130901 (2016).

[4] M. van Setten, M. Giantomassi, E. Bousquet, M. Verstraete, D. Hamann, X. Gonze, and G.-M. Rignanese, The pseudodojo: Training and grading a 85 element opti-

mized norm-conserving pseudopotential table, Computer Physics Communications **226**, 39 (2018).
[5] In the Quantum Espresso package v 6.7, the stress tensor calculation is not implemented for hybrid functionals.
[6] J. Rose, J. Ferrante, and J. Smith, Phys. Rev. B **47**, 675 (1981).
[7] T. Belytschko, S. Xiao, G. Schatz, and R. Ruoff, Phys. Rev. B **65**, 235430 (2002).
[8] B. Costescu, I. Baldus, and F. Gräter, Phys. Chem. Chem. Phys. **16**, 12591 (2014).
[9] F. Mouhat and F.-X. Coudert, Phys. Rev. B **90**, 224104 (2014).
[10] V. Kapil and et al., Comp. Phys. Comm. **236**, 214 (2019).
[11] T. T. Schneider, H. Beck, and E. Stoll, Phys. Rev. B **13**, 11233 (1976).
[12] S. Baroni, S. De Gironcoli, A. Dal Corso, and P. Giannozzi, Rev. Mod. Phys. **73**, 515 (2001).
[13] P. Ghosez, *Microscopic Properties of Ferroelectric Oxides from First-principles: Selected Topics : Part 1*, Troisième cycle de la physique en Suisse romande (EPFL, 2002).